Wave energy converter configuration in dual wave farms

Rafael J. Bergillos[a,*], Cristobal Rodriguez-Delgado[b,c], James Allen[b], Gregorio Iglesias[d,b]

[a] *Hydraulic Engineering Area, Department of Agronomy, University of Córdoba, Rabanales Campus, Leonardo Da Vinci Building, 14071 Córdoba, Spain*
[b] *School of Engineering, University of Plymouth, Plymouth PL4 8AA, UK*
[c] *PROES Consultores, Calle San Germán 39, 28020 Madrid, Spain*
[d] *MaREI, Environmental Research Institute & School of Engineering, University College Cork, College Road, Cork, Ireland*

Abstract

Wave farms, i.e., arrays of Wave Energy Converters (WECs), have recently been proven to be effective in fulfilling the dual function of carbon-free energy generation and coastal protection. In this paper these dual-function wave farms are referred as dual wave farms. The objective of this work is to investigate the influence of the WEC configuration on the performance of these dual wave farms through a case study: a dual wave farm consisting of WaveCat WECs deployed off an eroding beach. WaveCat is a floating overtopping WEC consisting of two hulls joined by their stern, forming a wedge. Two configurations are considered, with wedge angles of 30° and 60°. To characterize wave-WEC interaction, laboratory tests of a 1:30 WaveCat model are conducted using the two configurations and low-, mid- and high-energy sea states characteristic of the study area. The reflection and transmission coefficients obtained from the laboratory tests are inputted into a suite of numerical models to investigate the hydro- and morphodynamics of the beach. We find that the smaller wedge angle (30°) WECs afford more (less) coastal protection - quantified in terms of dry beach area availability - for short (long) peak periods than WECs with 60°. These results allow us to conclude that, for optimum performance of dual wave farms, WEC geometry should be adapted dynamically to the sea state.

*Corresponding author.
E-mail address: rafael.bergillos@uco.es (R.J. Bergillos)

Keywords: Ocean energy; wave farm; laboratory experiments; numerical modelling; device design

1. Introduction

The development of renewable energy is one of the most relevant targets confronting society in the coming decades [1, 2], due to the finite nature of fossil fuels, their high costs and, last but not least, the environmental impacts of their exploration and use [3, 4]. Among the carbon-free energy sources, marine energy resources offer a vast potential and comparatively low effects on the environment [5–9]. In particular, the worldwide potential of wave energy was assessed as 17 TW h/year [10]. These facts contrast with the low degree of development and utilization of wave energy compared to other renewable sources, such as hydroelectric, biomass or wind energy [11, 12].

For these reasons, increasing research efforts have focused on wave energy over the last years. The objectives of the investigations carried out so far have been: (1) the assessment and characterization of wave energy resources [13–25], (2) the study and optimization of possible locations [26–33], (3) the economic viability of wave energy [34–38], (4) the combined implementation with other ocean energies, most notably, wind [39–44], and (5) the development of wave energy technologies and devices [23, 45–63, 63–75].

One of the wave energy converters (WECs) under development is WaveCat [13, 76]. A floating, overtopping WEC, it comprises two hulls joined at the stern by a hinge – for a detailed description of the device, the reader is referred to [48, 77]. Wave farms consisting of WaveCat WECs have been proven to fulfil a dual function as wave energy generators and coastal defence elements on both sandy beaches [78–81] and gravel-dominated coasts [82–86].

So far, the effects of the WEC configuration on the hydro- and morphodynamics of the coast in the lee of the wave farm have not been studied. The main objective of the present research is to analyse the effects of the configuration of WaveCat, in particular, the wedge angle or angle between the twin hulls, on wave propagation, longshore sediment transport (LST) and shoreline dynamics, considering the varying transmission and reflection coefficients obtained from laboratory experiments under different sea states.

The laboratory experiments were conducted in the Ocean Basin of the University of Plymouth (Section 3.1). In addition, this research involved the application of a wave propagation model (Section 3.2.1), an LST formulation (Section 3.2.2) and a one-line model (Section 3.2.3) to a study site in southern Spain (Section 2).

2. Study site

Playa Granada is a gravel-dominated deltaic beach located on the Mediterranean coastline of southern Spain (Figure 1a). The beach, which is bounded by the Guadalfeo River mouth to the west and by *Punta del Santo* to the east (Figure 1b), has been experiencing shoreline retreat and terminal erosion in recent years [87–89], partly due to anthropogenic interventions in the Guadalfeo River basin [90–92].

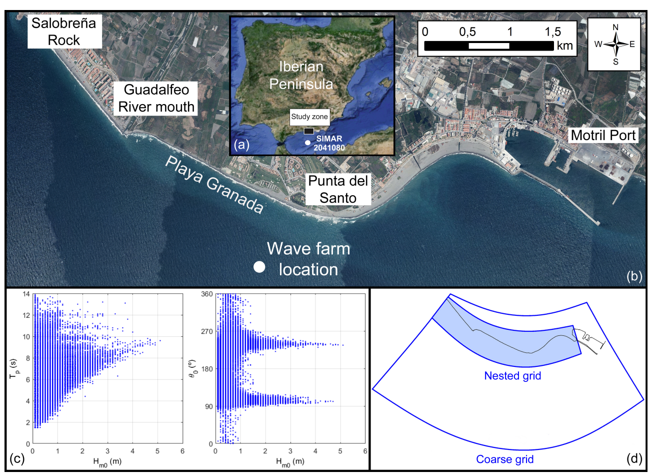

Figure 1: (a) Locations of the study zone and SIMAR point 2041080 in southern Iberian Peninsula. (b) Aerial image of the deltaic coast, indicating the wave farm location and the studied coastline section (Playa Granada). (c) Distributions H_{m0}-T_p and H_{m0}-θ_0 according to the SIMAR data. (d) Computational grids employed to apply the wave propagation model.

Two incoming wave directions are predominant at the study site (Figure 1c): south-west (SW) and south-east (SE). The values of deep-water significant wave height which are not exceeded 50%, 90%, 99% and 99.9% of the time are 0.5 m, 1.2 m, 2.1 m and 3.1 m, respectively [93]. The astronomical tidal range is ~ 0.6 m [94] and surge levels under storm conditions frequently exceed 0.5 m [95].

3. Methods

3.1. Laboratory experiments

Laboratory tests were performed in the Ocean Basin of the University of Plymouth to measure the reflection (K_r) and transmission (K_t) coefficients for two different wedge angles, i.e., angles between the hulls of WaveCat ($\alpha = 30°$ and $\alpha = 60°$, Figure 2). The experiments were carried out at a 1:30 scale and the dimensions of the model were 3 m (length) and 0.6 m (height) (Figure 2).

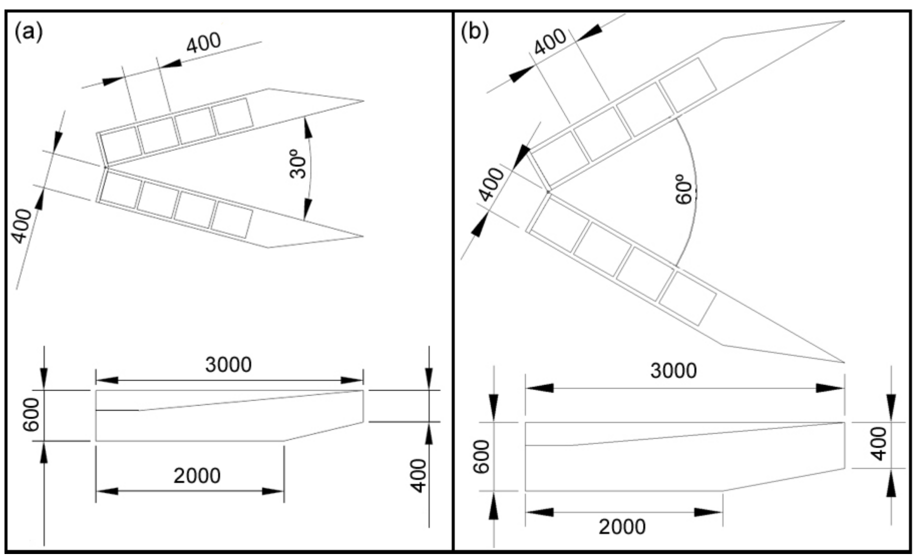

Figure 2: WEC configurations considered, model scale (dimensions in mm): (a) $\alpha = 30°$, (b) $\alpha = 60°$.

The selection of the two wedge angle values was done to represent two different types of operation of WaveCat corresponding to two different types of sea state: one in which the length of the incoming wave front that is harnessed by the device is maximised ($\alpha = 60°$), given that the wave power per linear metre of wave front is limited (low-energy sea state); and another in which the amount of wave power per linear meter of wave front is substantial (high-energy sea state), and therefore harnessing a shorter stretch of wave front is sufficient to reach the rated power of the device ($\alpha = 30°$).

Twelve different sea states were tested, with values of the significant wave height (H_{m0}) between 0.03 m and 0.1 m (1 m and 3 m) in the model (prototype). The tested values of the spectral peak period ($T_{p,\mathrm{mod}}$) ranged from 1.28 s to 2.37 s, representing real values ($T_{p,\mathrm{prot}}$) from 7 s to 13 s (Froude similarity). These sea states are representative of the wave conditions in Playa Granada (Figure 1c). The tested sea states, along with the measured reflection and transmission coefficients, are summarized in Table 1. A detailed description of the laboratory experiments can be found in [96, 97].

3.2. Numerical modelling

3.2.1. SWAN model

The SWAN model was used to propagate the sea states in the prototype scale, detailed in Section 3.1, from deep-water toward the coast for the two prevailing directions at the study zone (Figure 1c): SW (238°) and SE (107°). The model was previously calibrated for the study area by [98] through comparison with field data.

The wave farm location, shown in Figure 1b, was selected based on the results from previous studies, which have demonstrated that it is the best site in terms of wave energy potential [28] and coastal protection [84]. The wave farm layout, consisting of 11 WaveCat WECs spaced by a distance of 180 m and arranged in two rows, was also chosen on the basis of recent works at the study site [83, 85].

Test case	$H_{m0,\mathrm{mod}}$	$H_{m0,\mathrm{prot}}$ (m)	$T_{p,\mathrm{mod}}$ (s)	$T_{p,\mathrm{prot}}$ (s)	α (°)	K_r (-)	K_t (-)
S1_30	0.03	1	1.28	7	30	0.558	0.271
S2_30	0.03	1	1.64	9	30	0.436	0.368
S3_30	0.03	1	2.01	11	30	0.329	0.413
S4_30	0.03	1	2.37	13	30	0.268	0.441
S5_30	0.07	2	1.28	7	30	0.49	0.293
S6_30	0.07	2	1.64	9	30	0.399	0.363
S7_30	0.07	2	2.01	11	30	0.326	0.414
S8_30	0.07	2	2.37	13	30	0.266	0.439
S9_30	0.1	3	1.28	7	30	0.428	0.304
S10_30	0.1	3	1.64	9	30	0.361	0.359
S11_30	0.1	3	2.01	11	30	0.322	0.415
S12_30	0.1	3	2.37	13	30	0.265	0.437
S1_60	0.03	1	1.28	7	60	0.726	0.28
S2_60	0.03	1	1.64	9	60	0.499	0.359
S3_60	0.03	1	2.01	11	60	0.277	0.381
S4_60	0.03	1	2.37	13	60	0.213	0.387
S5_60	0.07	2	1.28	7	60	0.627	0.274
S6_60	0.07	2	1.64	9	60	0.351	0.342
S7_60	0.07	2	2.01	11	60	0.254	0.382
S8_60	0.07	2	2.37	13	60	0.186	0.399
S9_60	0.1	3	1.28	7	60	0.567	0.269
S10_60	0.1	3	1.64	9	60	0.399	0.336
S11_60	0.1	3	2.01	11	60	0.262	0.375
S12_60	0.1	3	2.37	13	60	0.189	0.396

Table 1: Wave conditions in the model ($H_{m0,\mathrm{mod}}$, $T_{p,\mathrm{mod}}$) and prototype ($H_{m0,\mathrm{prot}}$, $T_{p,\mathrm{prot}}$) scales, angle between hulls (α), reflection coefficient (K_r) and transmission coefficient (K_t) of the cases tested in the laboratory.

Two numerical grids were defined and used (Figure 1d): a coarse grid covering the entire deltaic region and extending from deep to shallow waters, and a nested grid covering the nearshore region, including the wave farm area, with higher resolution. To properly model the wave farm effects, the WECs were introduced in SWAN as artificial obstacles, specifying their reflection and transmission coefficients (hereafter denoted by K_r and K_t, respectively) for each sea state and wedge angle (Table 1). The results provided by SWAN were utilized to obtain wave variables at breaking conditions (through the fraction breaking variable) and, on this basis, apply the LST formulation below.

3.2.2. Longshore sediment transport formulation

LST was obtained through the formulation proposed by [99], which was found in previous work [98] to provide good estimates of the measured LST rates at the study site. The following expression was used:

$$Q = 0.00018 K \rho_s g^{0.5} (\tan\beta)^{0.4} (d_{50})^{-0.6} (H_{m,br})^{3.1} \sin(2\theta_{br}), \tag{1}$$

where Q is the LST rate, ρ_s is the sediment density, g the gravity acceleration, $\tan\beta$ the beach slope of the surf zone, d_{50} the grain size, $H_{m,br}$ (θ_{br}) the breaking significant wave height (wave angle respect to shore-normal) and the coefficient K considers the effect of wave period on LST.

3.2.3. One-line model

The LST rates obtained with the equation of [99] and detailed in the previous section were used to calculate the changes in the shoreline position through the application of a one-line model [100], which is based on the following equation:

$$\frac{\partial y_s}{\partial t} = -\frac{1}{D}\left(\frac{\partial Q}{\partial x_s}\right), \tag{2}$$

where y_s and x_s are the coordinates of the shoreline, t is the time, and D is the sum of the height of the berm and the closure depth. [98] proved that the joint application of the SWAN model, the LST formulation of [99] and the one-line model replicates the coastline changes in Playa Granada.

4. Results

4.1. Significant wave heights at breaking

This section details the influence of the wave farm on wave propagation – in particular, on the significant wave heights at breaking – depending on the wedge of the WECs. The alongshore variation of the differences between breaking significant wave heights for $\alpha = 30°$ and $\alpha = 60°$ ($\Delta H_{m,br}$) are indicated in Figure 3.

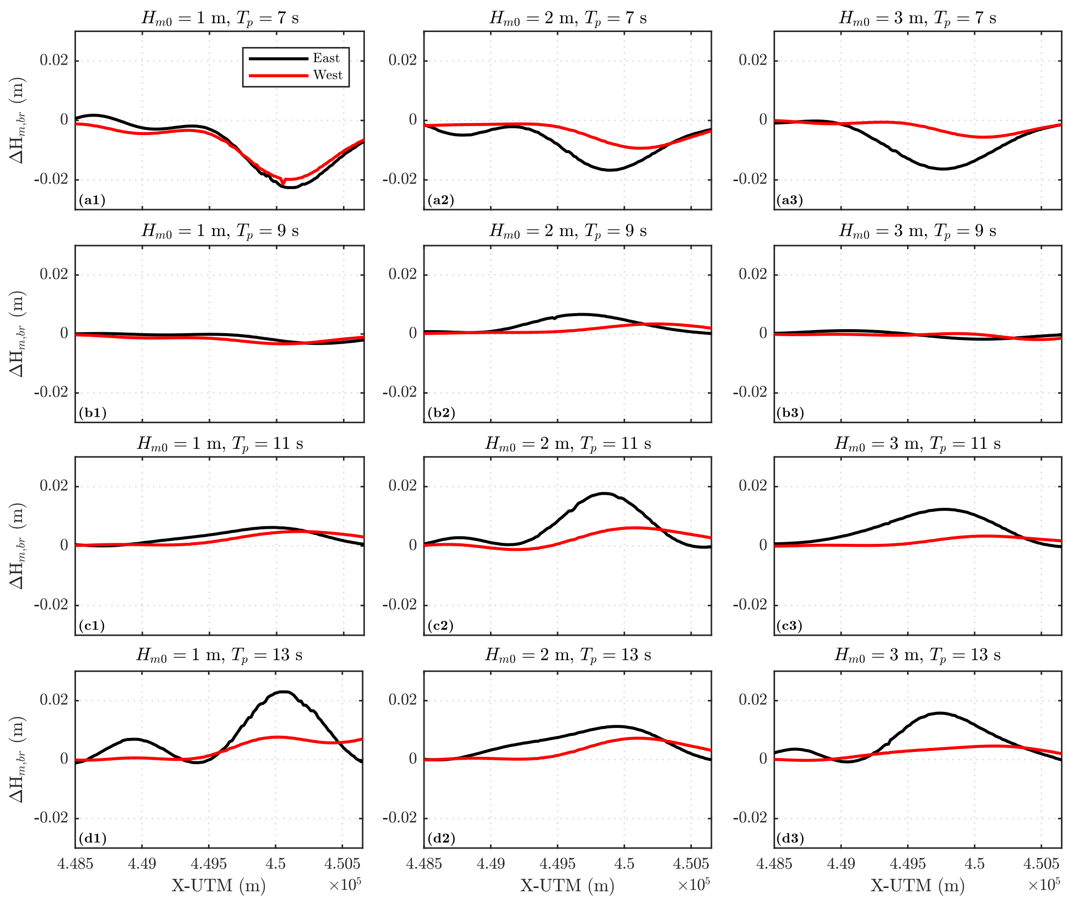

Figure 3: Alongshore distribution of the differences between the significant wave heights at breaking for $\alpha = 30°$ and $\alpha = 60°$ under SW (red) and SE (black) waves. [$\Delta H_{m,br} = H_{m,br,30} - H_{m,br,60}$].

Under SW waves, it is shown that the differences are generally negative for short wave periods ($T_p = 7$ s) and positive for long periods ($T_p = 11$ s and $T_p = 13$ s). In all the cases, the maximum differences are reached at the eastern part of the coast, influenced by the location of the wave farm (shown in Figure 1) and its effects in the leeward wave propagation patterns.

For all the H_{m0}, the alongshore-averaged values of $\Delta H_{m,br}$ for SW waves increase with increasing values of T_p (Figure 4). Thus, in terms of wave energy at the breaking zone, the wave farm composed by devices with the 30° configuration provides more (less) protection for short (long) T_p than that with the 60° configuration. This is a result of the different K_r and K_t of both configurations (Table 1). For given values of T_p, the differences in breaking wave heights between both angles decrease for increasing values of H_{m0} (Figure 4).

Under incoming SE waves, the differences are also negative (positive) for short (long) T_p, although in this case they extend along most of the study stretch (Figure 3). For constant values of H_{m0}, the alongshore-averaged $\Delta H_{m,br}$ under SE waves is greater for longer T_p (Figure 4); it is also due to the differences in K_r and K_t between both devices (Table 1). Thus, the greater the values of T_p, the lower the protection provided by devices with $\alpha = 30°$ compared to those with $\alpha = 60°$.

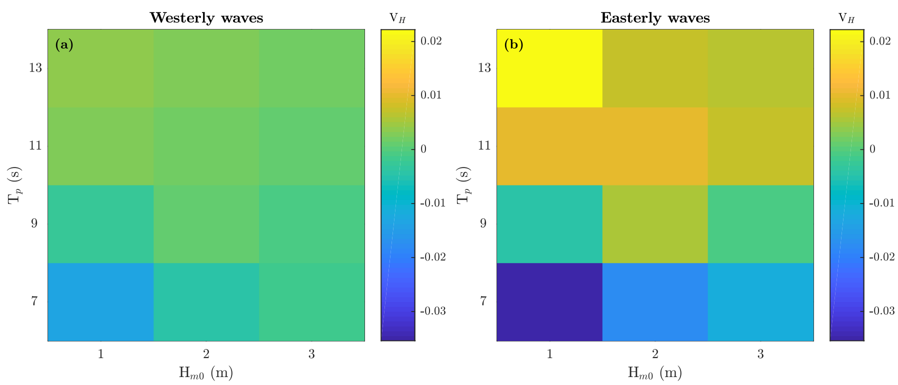

Figure 4: Variation in the alongshore-averaged significant wave heights at breaking for $\alpha = 30°$ with respect to the values for $\alpha = 60°$ under SW (a) and SE (b) waves. $[V_H = (\bar{H}_{m,br,30} - \bar{H}_{m,br,60})/\bar{H}_{m,br,30}]$.

The differences in significant wave height at breaking between both devices under SE wave conditions are generally greater than those under SW waves (Figure 4); with maximum negative (positive) alongshore-averaged values of $\Delta H_{m,br}$ equal to -0.82 cm (0.77 cm) for low-energy waves (H_{m0}=1 m), -0.77 cm (0.55 cm) for mid-energy waves (H_{m0}=2 m), and -0.71 cm (0.61 cm) for high-energy waves (H_{m0}=3 m).

4.2. Longshore sediment transport rates

The differences in LST rates between the WECs with $\alpha = 30°$ and $\alpha = 60°$ are analysed in this section. Figure 5 depicts the alongshore distribution of these differences for all the sea states considered. Under SW waves, the differences are generally greater for higher values of $H_{m,0}$ and lower values of T_p, i.e. the greater the wave steepness, the higher the differences in LST rates between the farms with both angles. The differences are more significant in the western (eastern) stretch of the coast for short (long) peak periods (Figure 5).

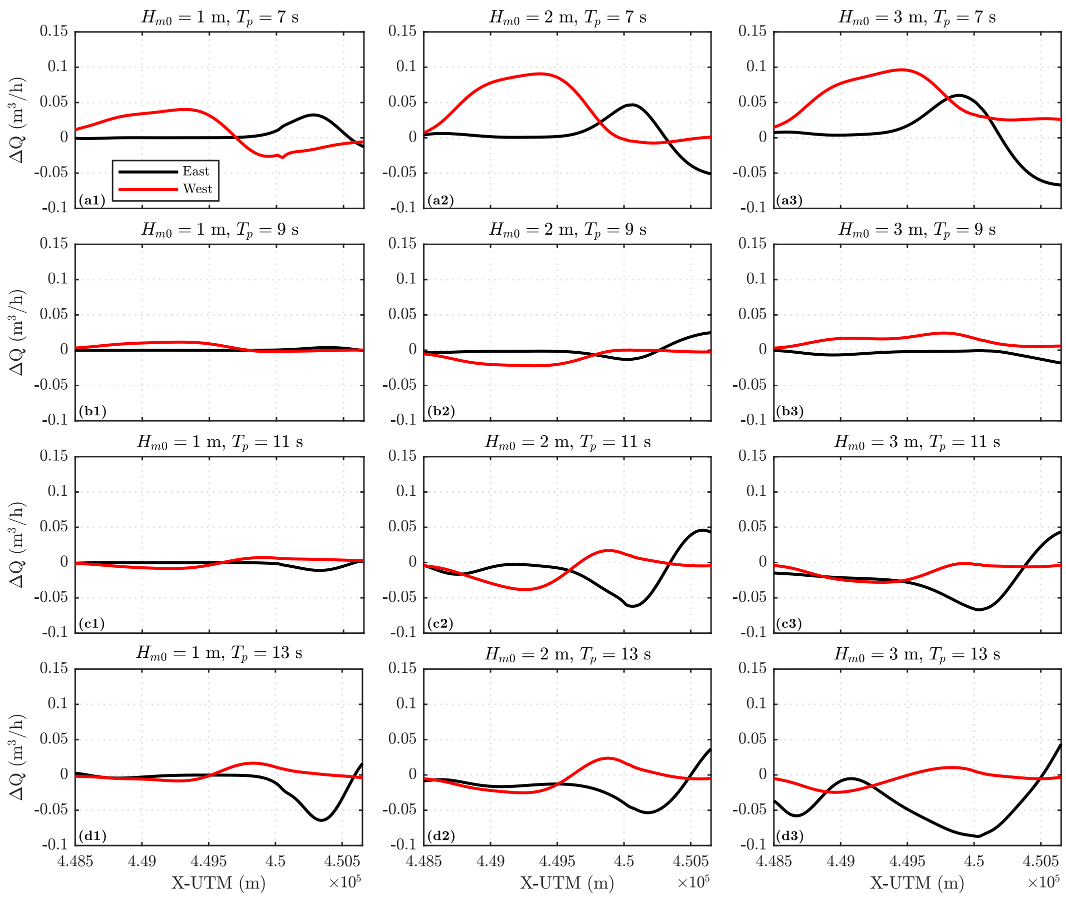

Figure 5: Alongshore distribution of the differences between the LST rates for $\alpha = 30°$ and $\alpha = 60°$ under SW (red) and SE (black) waves. $[\Delta Q = Q_{30} - Q_{60}]$.

Under SE wave conditions, the greater differences are located in the eastern part of the study section (Figure 5), i.e., in the lee of the wave farm (Figure 1). For short periods ($T_p = 7$ s), the differences are negative in the eastern end of the stretch of beach and become positive toward the west; whereas the opposite occurs for long periods ($T_p = 11$ s and $T_p = 13$ s). In general, the differences are greater as the $H_{m,0}$ values increase (Table 2).

	SW waves			SE waves		
	H_{m0}=1 m	H_{m0}=2 m	H_{m0}=3 m	H_{m0}=1 m	H_{m0}=2 m	H_{m0}=3 m
T_p=7 s	-0.0092	-0.0385	-0.0548	-0.0055	-0.0052	-0.0073
T_p=9 s	-0.0045	0.0105	-0.0136	-0.0006	0.001	0.0044
T_p=11 s	0.0006	0.0104	0.0134	0.002	0.0128	0.0256
T_p=13 s	-0.0007	0.0054	0.0062	0.0116	0.0185	0.0425

Table 2: Differences between the alongshore-averaged LST rates for $\alpha = 30°$ and $\alpha = 60°$ under SW and SE waves (in m^3/h).

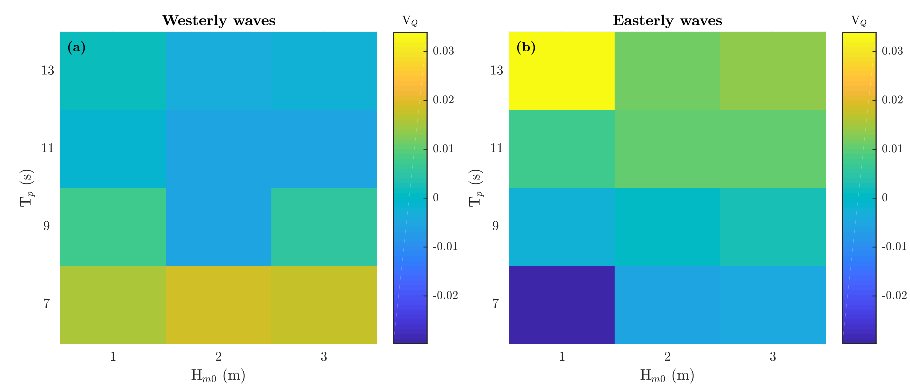

Figure 6: Variation in the alongshore-averaged LST rates for $\alpha = 30°$ with respect to the values for $\alpha = 60°$ under SW (a) and SE (b) waves. [$V_Q = (\bar{Q}_{30} - \bar{Q}_{60})/\bar{Q}_{30}$].

The differences in LST rates between the farms composed by both devices under SE wave conditions are greater than those under SW waves (Table 2 and Figure 6). This is influenced by both the higher differences in breaking significant wave heights (Section 4.1) and the higher angles from shore-normal for SE waves, which increase the LST rates and differences.

4.3. Shoreline geometry

The LST rates obtained in the previous section were used to compute the variations in the shoreline morphology over a one-month period for $H_{m,0}$=1 m, $H_{m,0}$=2 m and $H_{m,0}$=3 m, representing low-, mid- and high-energy conditions, respectively. The differences between the final shorelines for $\alpha = 30°$ and $\alpha = 60°$ under both SW and SE waves are shown in Figure 7.

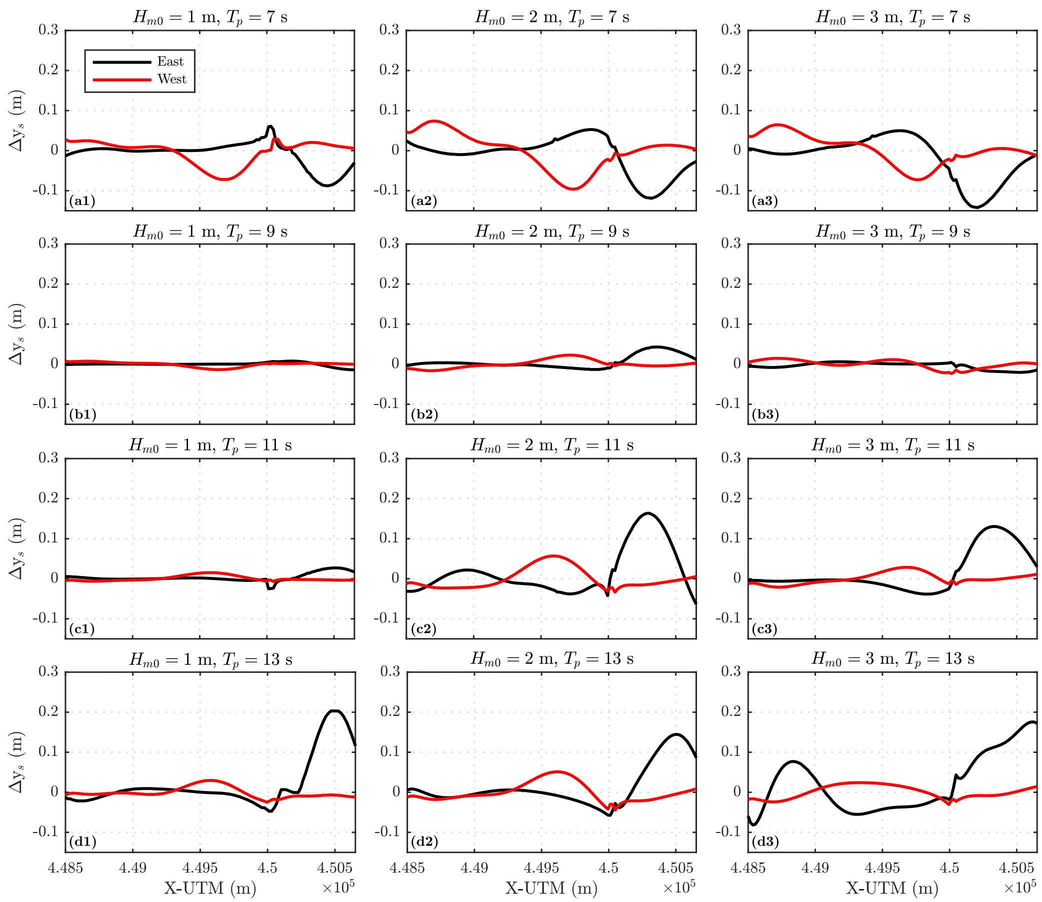

Figure 7: Alongshore distribution of the the differences between the final coastline positions (after 1 month) for $\alpha = 30°$ and $\alpha = 60°$ under SW (red) and SE (black) waves. [$\Delta y = y_{\text{final},30} - y_{\text{final},60}$].

For SW waves and short peak periods (T_p=7 s), the maximum differences are negative and concentrated in the central stretch of beach (where the main occupations are located), indicating that the wave farm with $\alpha = 30°$ provides greater protection at this location. On the contrary, the differences in the western part of the beach are positive (Figure 7), i.e., the farm with $\alpha = 60°$ leads to greater accretion near the river mouth for short wave periods. This section has experienced acute shoreline retreat in recent years due to river damming [91].

For long wave periods (T_p=11 s and T_p=13 s), the maximum differences under SW waves are positive and located in the central stretch of beach. In addition, the alongshore-averaged values are positive for low-, mid- and high-energy conditions (Table 3). Thus, under SW waves with long periods, the wave farm with $\alpha = 60°$ provides greater protection against shoreline erosion. This leads to a higher efficiency in terms of dry beach area (Section 4.4).

	SW waves			SE waves		
	H_{m0}=1 m	H_{m0}=2 m	H_{m0}=3 m	H_{m0}=1 m	H_{m0}=2 m	H_{m0}=3 m
T_p=7 s	-0.36	-0.06	0.21	-0.66	-1.06	- 1.65
T_p=9 s	-0.04	-0.04	0.02	0.01	0.54	0.39
T_p=11 s	0.05	0.05	0.01	0.3	1.65	1.48
T_p=13 s	0.1	0.06	0.03	2.1	1.23	2.01

Table 3: Differences between the alongshore-averaged final coastline positions for $\alpha = 30°$ and $\alpha = 60°$ under SW and SE waves (in cm).

On the other hand, under SE waves, the greatest differences are concentrated along the eastern section of the coastline. This is caused by the farm location (Figure 1) and the resulting greater differences in LST between both angles at this stretch of beach (Figure 5). The differences in final shoreline positions are generally negative (positive) for short (long) peak periods, indicating that the wave farm composed by WECs with $\alpha = 30°$ ($\alpha = 60°$) provides more protection for short (long) wave periods (Figure 5 and Table 3).

For all the sea states considered, the differences in the final shoreline geometries between devices with $\alpha = 30°$ and $\alpha = 60°$ under SE wave conditions are higher than those under SW waves. These differences determine the dry beach area availability, as explained in the following section.

4.4. Dry beach area

The differences between the final and initial dry beach areas for all the sea states analysed and for both angles between the hulls are depicted in Figure 8. It may be observed that these differences are always positive, i.e., beach accretion occurs in all cases. This confirms the efficiency of wave farms as protection elements against coastline erosion.

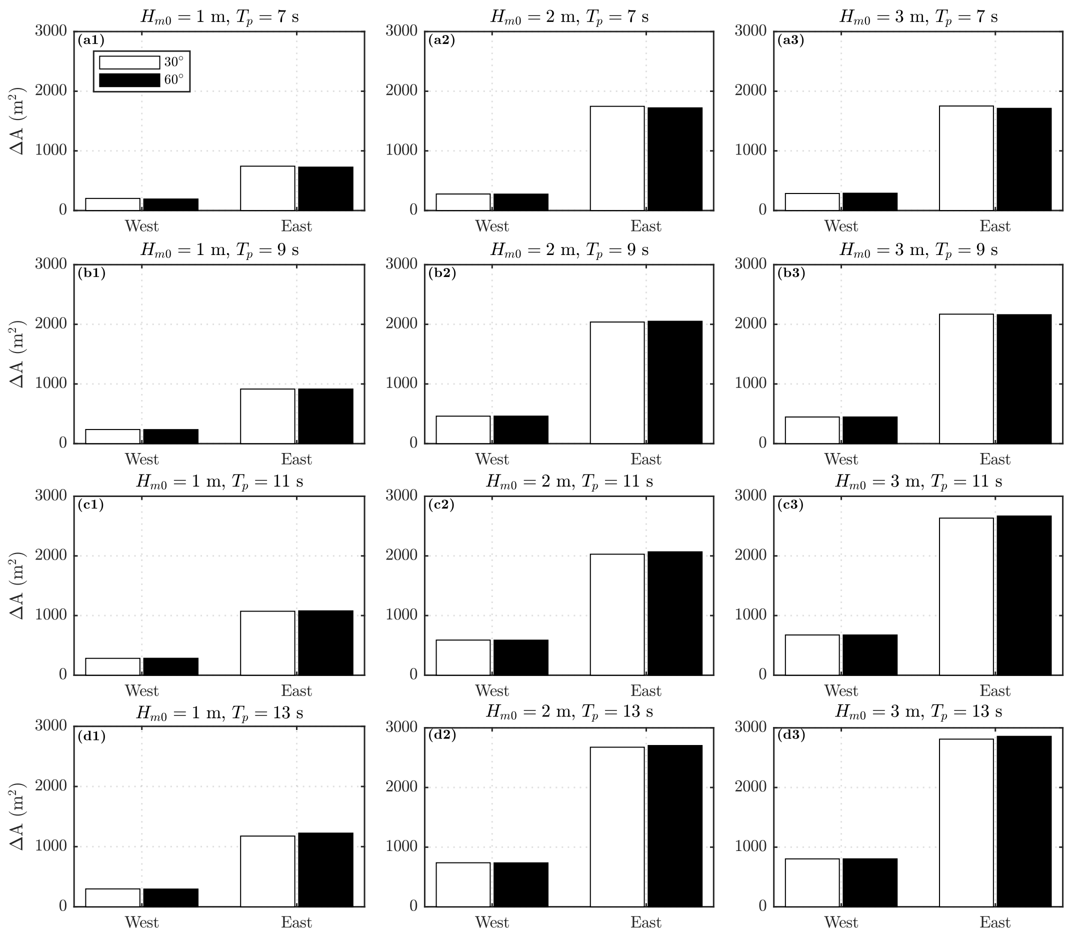

Figure 8: Dry beach area variations for $\alpha = 30°$ (white) and $\alpha = 60°$ (black) under SW and SE waves. [$\Delta A = A_{\text{final}} - A_{\text{initial}}$].

As shown in Figure 8, the accretion is more pronounced under SE waves. This is in agreement with the observed morphological response of the coastline, since SW waves contribute to erode the beach and SE waves lead to beach recovery [98, 101]. In this case, the presence of the farm increases the beach accretion under SE waves and reverts the coastline response (from erosion to accretion) under SW wave conditions. The dry beach area differences are generally greater with increasing values of H_{m0} and T_p (Figure 8).

The comparison of the results obtained for both angles between hulls allow concluding that, under SW waves, the farm composed by devices with $\alpha = 60°$ is more efficient in terms of coastal protection for all the cases except four of them (associated to mild conditions): H_{m0}=1 m - T_p=7 s, H_{m0}=1 m - T_p=9 s, H_{m0}=2 m - T_p=7 s and H_{m0}=2 m - T_p=9 s (Table 4 and Figure 9). Under SE waves, the WaveCat devices with $\alpha = 30°$ are more efficient for the shortest peak period (T_p=7 s), whereas those with $\alpha = 60°$ lead to greater accretion values for the rest of wave conditions (Table 4).

	SW waves			SE waves		
	H_{m0}=1 m	H_{m0}=2 m	H_{m0}=3 m	H_{m0}=1 m	H_{m0}=2 m	H_{m0}=3 m
T_p=7 s	9.4	1.8	-4.7	15.4	26	39
T_p=9 s	1	0.9	-0.5	-0.5	-13	-9
T_p=11 s	-1.3	-1.1	-0.1	-7	-41	-36
T_p=13 s	-2.3	-1.4	-0.7	-49	-29	-47

Table 4: Differences between the final dry beach area for $\alpha = 30°$ and $\alpha = 60°$ under SW and SE waves (in m^2).

The results of this section indicate that, for the best performance in terms of coastal protection, the geometry of the WECs should be adjusted dynamically to the sea state. If this is not possible, i.e., if a fixed configuration (constant wedge angle) must be adopted, then this configuration should be chosen on the basis of a detailed analysis of the wave climate at the site of interest, with a view to optimizing the coastal protection performance under the prevailing sea states.

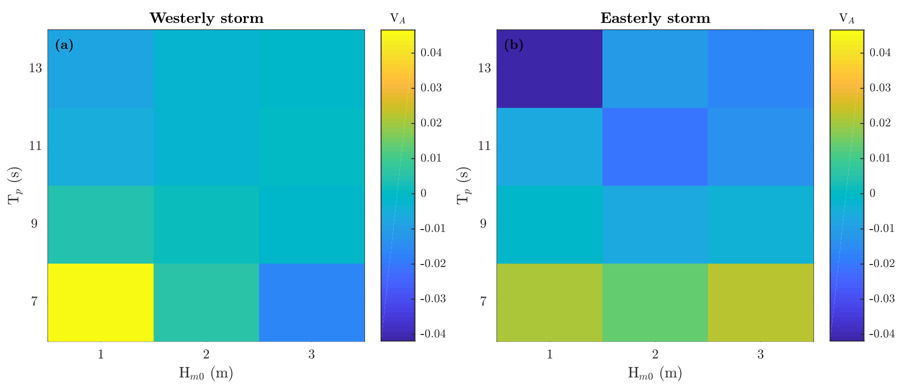

Figure 9: Variation in the dry beach area differences for $\alpha = 30°$ with respect to the values for $\alpha = 60°$ under SW (a) and SE (b) waves. $[V_A = (\Delta A_{30} - \Delta A_{60})/\Delta A_{30}]$.

The methodology presented in this work, which combines laboratory tests with different WEC configurations and numerical modelling, may be used for other geometries and beaches to investigate the optimum configuration for a wave farm project.

5. Conclusions

Wave energy is one of the renewables with the greatest potential for development due to the resource availability and low visual pollution. Recent research has highlighted the possibility of using wave farms for a dual function, i.e., renewable energy generation and coastal protection.

This paper presents the first study on the influence of WEC configuration on the performance of dual wave farms. In particular, the effects of two values of the wedge angle, i.e., the angle between the twin hulls of WaveCat WECs ($\alpha = 30°$ and $\alpha = 60°$) on significant wave height at breaking, LST rates, shoreline geometry and dry beach area were analysed. For this purpose, the transmission and reflection coefficients were determined for relevant sea states based on laboratory experiments in a wave tank, and these values were used to model the wave farm-induced morphological variations on a gravel-dominated beach.

The results indicate that, under both SW and SE waves, the wave farm composed by WaveCat devices with $\alpha = 30°$ provides more (less) protection for short (long) peak periods, quantified in terms of breaking wave heights. This is down to the different values of the transmission and reflection coefficients corresponding to the two configurations. The differences in significant wave height at breaking between the two WEC configurations under SE waves are generally greater than those under SW waves. This, along with the more oblique incidence for SE waves, leads to greater differences in LST rates between the two configurations under SE waves.

The LST rates thus obtained were used to compute the changes in shoreline geometry and dry beach area. The results confirm the efficiency of wave farms in coastal protection indeed, accretion occurs under all the sea states considered. The gains in dry beach area obtained with the 60° WEC configuration were generally greater for long peak periods (T_p=11 s and T_p=13 s) and lower for the shortest peak period (T_p=7 s). We conclude that the performance of dual wave farms depends on both the WEC configuration and the sea state. In other words, the optimum configuration depends on the sea state.

Therefore, for maximum performance of the wave farm in coastal erosion protection, the WEC geometry should be adjusted dynamically to the sea state. This dynamic adaptation strategy leads to a greater dry beach area. With the methodology presented in this paper, this benefit may be quantified for any beach of interest, and compared with the cost of the dynamic adaptation strategy versus a constant geometry strategy in order to establish which is more appropriate. Future research should focus on the assessment of the role of WEC configuration in power production, investigating the optimum pair angle-draft that maximises power production.

Acknowledgements

This paper was carried out in the framework of research grants WAVEIMPACT (PCIG-13-GA-2013-618556, European Commission, Marie Curie fellowship, fellow GI) and ICE (Intelligent Community Energy, European Commision, Contract no. 5025). RB was funded by the Spanish Ministry of Science, Innovation and Universities (*Programa Juan de la Cierva 2017*, FJCI-2017-31781). Wave and bathymetric data were provided by *Puertos del Estado* (Spain) and the Spanish Ministry of Agriculture, Fisheries and Food, respectively. We thank two anonymous reviewers for their improvements to this work.

References

[1] European Commission, A European Strategic Energy Technology Plan (Set-Plan): Towards a low carbon future, Brussels: Commission of the European Communities (2007).

[2] European Commission, Renewable Energy Directive 2009/28/EC , European Union, 2009.

[3] M. Asif, T. Muneer, Energy supply, its demand and security issues for developed and emerging economies, Renewable and Sustainable Energy Reviews 11 (2007) 1388–1413.

[4] S. Shafiee, E. Topal, When will fossil fuel reserves be diminished?, Energy policy 37 (2009) 181–189.

[5] J. Falnes, A review of wave-energy extraction, Marine Structures 20 (2007) 185–201.

[6] A. M. Cornett, A global wave energy resource assessment, in: The Eighteenth International Offshore and Polar Engineering Conference, International Society of Offshore and Polar Engineers, 2008.

[7] J. Cruz, Ocean wave energy: current status and future perspectives, Springer Science & Business Media, 2008.

[8] N. Panwar, S. Kaushik, S. Kothari, Role of renewable energy sources in environmental protection: a review, Renewable and Sustainable Energy Reviews 15 (2011) 1513–1524.

[9] G. Rinaldi, P. Thies, R. Walker, L. Johanning, A decision support model to optimise the operation and maintenance strategies of an offshore renewable energy farm, Ocean Engineering 145 (2017) 250–262.

[10] H. Lund, Renewable energy strategies for sustainable development, Energy 32 (2007) 912–919.

[11] U. E. I. Administration, et al., Annual Energy Outlook 2011: With Projections to 2035, Government Printing Office, 2011.

[12] Eurostat, Renewable energy statistics, European Union, 2016.

[13] G. Iglesias, R. Carballo, A. Castro, B. Fraga, Development and design of the WaveCat$^{\mathrm{TM}}$ energy converter, in: Coastal Engineering 2008: (In 5 Volumes), World Scientific, 2009, pp. 3970–3982.

[14] G. Iglesias, R. Carballo, Choosing the site for the first wave farm in a region: A case study in the Galician Southwest (Spain), Energy 36 (2011) 5525–5531.

[15] D. Vicinanza, P. Contestabile, V. Ferrante, Wave energy potential in the north-west of Sardinia (Italy), Renewable Energy 50 (2013) 506–521.

[16] R. Carballo, M. Sánchez, V. Ramos, J. Fraguela, G. Iglesias, The intra-annual variability in the performance of wave energy converters: A comparative study in N Galicia (Spain), Energy 82 (2015) 138 – 146.

[17] P. Contestabile, V. Ferrante, D. Vicinanza, Wave energy resource along the coast of Santa Catarina (Brazil), Energies 8 (2015) 14219–14243.

[18] M. López, M. Veigas, G. Iglesias, On the wave energy resource of Peru, Energy Conversion and Management 90 (2015) 34 – 40.

[19] D. Silva, A. R. Bento, P. Martinho, C. G. Soares, High resolution local wave energy modelling in the Iberian Peninsula, Energy 91 (2015) 1099–1112.

[20] M. Veigas, M. López, G. Iglesias, Assessing the optimal location for a shoreline wave energy converter, Applied Energy 132 (2014) 404 – 411.

[21] M. Veigas, M. López, P. Romillo, R. Carballo, A. Castro, G. Iglesias, A proposed wave farm on the galician coast, Energy Conversion and Management 99 (2015) 102–111.

[22] C. Iuppa, L. Cavallaro, D. Vicinanza, E. Foti, Investigation of suitable sites for Wave Energy Converters around Sicily (Italy)., Ocean Science Discussions 12 (2015).

[23] A. Viviano, S. Naty, E. Foti, T. Bruce, W. Allsop, D. Vicinanza, Large-scale experiments on the behaviour of a generalised oscillating water column under random waves, Renewable Energy 99 (2016) 875 – 887.

[24] R. Carballo, N. Arean, M. Álvarez, I. López, A. Castro, M. López, G. Iglesias, Wave farm planning through high-resolution resource and performance characterization, Renewable Energy (2018).

[25] L. F. Prieto, G. R. Rodríguez, J. S. Rodríguez, Wave energy to power a desalination plant in the north of Gran Canaria Island: Wave resource, socioeconomic and environmental assessment, Journal of Environmental Management 231 (2019) 546–551.

[26] R. Carballo, M. Sánchez, V. Ramos, F. Taveira-Pinto, G. Iglesias, A high resolution geospatial database for wave energy exploitation, Energy 68 (2014) 572 – 583.

[27] C. Iuppa, L. Cavallaro, E. Foti, D. Vicinanza, Potential wave energy production by different wave energy converters around Sicily, Journal of Renewable and Sustainable Energy 7 (2015) 061701.

[28] A. López-Ruiz, R. J. Bergillos, M. Ortega-Sánchez, The importance of wave climate forecasting on the decision-making process for nearshore wave energy exploitation, Applied Energy 182 (2016) 191 – 203.

[29] N. Elginoz, B. Bas, Life Cycle Assessment of a multi-use offshore platform: Combining wind and wave energy production, Ocean Engineering 145 (2017) 430–443.

[30] I. Alifdini, N. A. P. Iskandar, A. W. Nugraha, D. N. Sugianto, A. Wirasatriya, A. B. Widodo, Analysis of ocean waves in 3 sites potential areas for renewable energy development in Indonesia, Ocean Engineering 165 (2018) 34–42.

[31] D. Khojasteh, S. M. Mousavi, W. Glamore, G. Iglesias, Wave energy status in asia, Ocean Engineering 169 (2018) 344–358.

[32] A. López-Ruiz, R. J. Bergillos, A. Lira-Loarca, M. Ortega-Sánchez, A methodology for the long-term simulation and uncertainty analysis of the operational lifetime performance of wave energy converter arrays, Energy 153 (2018) 126–135.

[33] A. López-Ruiz, R. J. Bergillos, J. M. Raffo-Caballero, M. Ortega-Sánchez, Towards an optimum design of wave energy converter arrays through an integrated approach of life cycle performance and operational capacity, Applied Energy 209 (2018) 20 – 32.

[34] S. Astariz, G. Iglesias, The economics of wave energy: A review, Renewable and Sustainable Energy Reviews 45 (2015) 397 – 408.

[35] S. Astariz, A. Vazquez, G. Iglesias, Evaluation and comparison of the levelized cost of tidal, wave, and offshore wind energy, Journal of Renewable and Sustainable Energy 7 (2015) 053112.

[36] S. Astariz, G. Iglesias, Wave energy vs. other energy sources: A reassessment of the economics, International Journal of Green Energy 13 (2016) 747–755.

[37] P. Contestabile, E. Di Lauro, M. Buccino, D. Vicinanza, Economic Assessment of Overtopping BReakwater for Energy Conversion (OBREC): A Case Study in Western Australia, Sustainability 9 (2017) 51.

[38] C. Frost, D. Findlay, E. Macpherson, P. Sayer, L. Johanning, A model to map levelised cost of energy for wave energy projects, Ocean Engineering 149 (2018) 438–451.

[39] A. Azzellino, V. Ferrante, J. P. Kofoed, C. Lanfredi, D. Vicinanza, Optimal siting of offshore wind-power combined with wave energy through a marine spatial planning approach, International Journal of Marine Energy 3 (2013) e11–e25.

[40] S. Astariz, G. Iglesias, Enhancing wave energy competitiveness through co-located wind and wave energy farms. a review on the shadow effect, Energies 8 (2015) 7344–7366.

[41] S. Astariz, J. Abanades, C. Perez-Collazo, G. Iglesias, Improving wind farm accessibility for operation and maintenance through a co-located wave farm: Influence of layout and wave climate, Energy Conversion and Management 95 (2015) 229 – 241.

[42] S. Astariz, G. Iglesias, Output power smoothing and reduced downtime period by combined wind and wave energy farms, Energy 97 (2016) 69 – 81.

[43] C. Pérez-Collazo, D. Greaves, G. Iglesias, A review of combined wave and offshore wind energy, Renewable and Sustainable Energy Reviews 42 (2015) 141 – 153.

[44] Z. Wang, C. Duan, S. Dong, Long-term wind and wave energy resource assessment in the South China sea based on 30-year hindcast data, Ocean Engineering 163 (2018) 58–75.

[45] D. Vicinanza, L. Margheritini, J. P. Kofoed, M. Buccino, The SSG wave energy converter: Performance, status and recent developments, Energies 5 (2012) 193–226.

[46] A. F. de O. Falcão, Modelling and control of oscillating-body wave energy converters with hydraulic power take-off and gas accumulator, Ocean Engineering 34 (2007) 2021–2032.

[47] L. Margheritini, D. Vicinanza, P. Frigaard, SSG wave energy converter: Design, reliability and hydraulic performance of an innovative overtopping device, Renewable Energy 34 (2009) 1371–1380.

[48] H. Fernandez, G. Iglesias, R. Carballo, A. Castro, J. Fraguela, F. Taveira-Pinto, M. Sanchez, The new wave energy converter WaveCat: Concept and laboratory tests, Marine Structures 29 (2012) 58–70.

[49] D. Vicinanza, J. H. Nørgaard, P. Contestabile, T. L. Andersen, Wave loadings acting on overtopping breakwater for energy conversion, Journal of Coastal Research 65 (2013) 1669–1674.

[50] I. López, B. Pereiras, F. Castro, G. Iglesias, Optimisation of turbine-induced damping for an OWC wave energy converter using a RANS–VOF numerical model, Applied Energy 127 (2014) 105 – 114.

[51] I. López, G. Iglesias, Efficiency of OWC wave energy converters: A virtual laboratory, Applied Ocean Research 44 (2014) 63 – 70.

[52] D. Vicinanza, P. Contestabile, J. Q. H. Nørgaard, T. L. Andersen, Innovative rubble mound breakwaters for overtopping wave energy conversion, Coastal Engineering 88 (2014) 154–170.

[53] A. Day, A. Babarit, A. Fontaine, Y.-P. He, M. Kraskowski, M. Murai, I. Penesis, F. Salvatore, H.-K. Shin, Hydrodynamic modelling of marine renewable energy devices: A state of the art review, Ocean Engineering 108 (2015) 46–69.

[54] I. López, B. Pereiras, F. Castro, G. Iglesias, Performance of OWC wave energy converters: Influence of turbine damping and tidal variability, International Journal of Energy Research 39 (2015) 472–483. ER-13-4164.R2.

[55] I. López, A. Castro, G. Iglesias, Hydrodynamic performance of an oscillating water column wave energy converter by means of particle imaging velocimetry, Energy 83 (2015) 89 – 103.

[56] I. López, B. Pereiras, F. Castro, G. Iglesias, Holistic performance analysis and turbine-induced damping for an owc wave energy converter, Renewable Energy 85 (2016) 1155–1163.

[57] M. Buccino, D. Stagonas, D. Vicinanza, Development of a composite sea wall wave energy converter system, Renewable Energy 81 (2015) 509–522.

[58] P. Contestabile, C. Iuppa, E. Di Lauro, L. Cavallaro, T. L. Andersen, D. Vicinanza, Wave loadings acting on innovative rubble mound breakwater for overtopping wave energy conversion, Coastal Engineering 122 (2017) 60–74.

[59] A. Elhanafi, G. Macfarlane, A. Fleming, Z. Leong, Experimental and numerical investigations on the hydrodynamic performance of a floating-moored oscillating water column wave energy converter, Applied Energy 205 (2017) 369 – 390.

[60] M. López, F. Taveira-Pinto, P. Rosa-Santos, Numerical modelling of the ceco wave energy converter, Renewable Energy 113 (2017) 202–210.

[61] M. López, F. Taveira-Pinto, P. Rosa-Santos, Influence of the power take-off characteristics on the performance of ceco wave energy converter, Energy 120 (2017) 686–697.

[62] E. Medina-López, R. Bergillos, A. Moñino, M. Clavero, M. Ortega-Sánchez, Effects of seabed morphology on oscillating water column wave energy converters, Energy 135 (2017) 659–673.

[63] M. López, V. Ramos, P. Rosa-Santos, F. Taveira-Pinto, Effects of the PTO inclination on the performance of the CECO wave energy converter, Marine Structures 61 (2018) 452–466.

[64] A. Moñino, E. Medina-López, R. J. Bergillos, M. Clavero, A. Borthwick, M. Ortega-Sánchez, Thermodynamics and Morphodynamics in Wave Energy, Springer, 2018.

[65] V. Ramos, M. López, F. Taveira-Pinto, P. Rosa-Santos, Performance assessment of the ceco wave energy converter: Water depth influence, Renewable Energy 117 (2018) 341–356.

[66] E. Medina-López, A. Moñino, R. Bergillos, M. Clavero, M. Ortega-Sánchez, Oscillating water column performance under the influence of storm development, Energy 166 (2019) 765–774.

[67] O. Barambones, J. A. Cortajarena, J. M. G. de Durana, P. Alkorta, A real time sliding mode control for a wave energy converter based on a wells turbine, Ocean Engineering 163 (2018) 275–287.

[68] Z. Chao, Y. Yage, C. Aiju, Hydrodynamics research of a two-body articulated wave energy device, Ocean Engineering 148 (2018) 202–210.

[69] H.-T. Do, T.-D. Dang, K. K. Ahn, A multi-point-absorber wave-energy converter for the stabilization of output power, Ocean Engineering 161 (2018) 337–349.

[70] P. Halder, M. H. Mohamed, A. Samad, Wave energy conversion: Design and shape optimization, Ocean Engineering 150 (2018) 337–351.

[71] A. Kolios, L. F. Di Maio, L. Wang, L. Cui, Q. Sheng, Reliability assessment of point-absorber wave energy converters, Ocean Engineering 163 (2018) 40–50.

[72] N. Sergiienko, A. Rafiee, B. Cazzolato, B. Ding, M. Arjomandi, Feasibility study of the three-tether axisymmetric wave energy converter, Ocean Engineering 150 (2018) 221–233.

[73] B. Wu, M. Li, R. Wu, T. Chen, Y. Zhang, Y. Ye, BBDB wave energy conversion technology and perspective in China, Ocean Engineering 169 (2018) 281–291.

[74] Y. Yang, I. Diaz, M. Morales, A vertical-axis unidirectional rotor for wave energy conversion, Ocean Engineering 160 (2018) 224–230.

[75] S. Zheng, Y. Zhang, Analytical study on wave power extraction from a hybrid wave energy converter, Ocean Engineering 165 (2018) 252–263.

[76] G. Iglesias, H. Fernándes, R. Carballo, A. Castro, F. Taveira-Pinto, The wavecat©-development of a new wave energy converter, in: World Renewable Energy Congress-Sweden; 8-13 May; 2011; Linköping; Sweden, 57, Linköping University Electronic Press, 2011, pp. 2151–2158.

[77] H. Fernandez, G. Iglesias, R. Carballo, A. Castro, M. Sánchez, F. Taveira-Pinto, Optimization of the wavecat wave energy converter, Coastal Engineering Proceedings 1 (2012) 5.

[78] J. Abanades, D. Greaves, G. Iglesias, Wave farm impact on the beach profile: A case study, Coastal Engineering 86 (2014) 36–44.

[79] J. Abanades, D. Greaves, G. Iglesias, Coastal defence through wave farms, Coastal Engineering 91 (2014) 299–307.

[80] J. Abanades, D. Greaves, G. Iglesias, Coastal defence using wave farms: The role of farm-to-coast distance, Renewable Energy 75 (2015) 572–582.

[81] J. Abanades, G. Flor-Blanco, G. Flor, G. Iglesias, Dual wave farms for energy production and coastal protection, Ocean & Coastal Management 160 (2018) 18 – 29.

[82] R. J. Bergillos, A. Lopez-Ruiz, E. Medina-Lopez, A. Monino, M. Ortega-Sanchez, The role of wave energy converter farms on coastal protection in eroding deltas, Guadalfeo, southern Spain, Journal of Cleaner Production 171 (2018) 356–367.

[83] C. Rodriguez-Delgado, R. J. Bergillos, M. Ortega-Sánchez, G. Iglesias, Protection of gravel-dominated coasts through wave farms: Layout and shoreline evolution, Science of The Total Environment 636 (2018) 1541–1552.

[84] C. Rodriguez-Delgado, R. J. Bergillos, M. Ortega-Sánchez, G. Iglesias, Wave farm effects on the coast: The alongshore position, Science of The Total Environment 640 (2018) 1176–1186.

[85] C. Rodriguez-Delgado, R. J. Bergillos, G. Iglesias, Dual wave energy converter farms and coastline dynamics: the role of inter-device spacing, Science of The Total Environment, 646 (2019) 1241–1252.

[86] R. J. Bergillos, C. Rodriguez-Delgado, G. Iglesias, Wave farm impacts on coastal flooding under sea-level rise: a case study in southern Spain, Science of the Total Environment 653 (2019) 1522–1531.

[87] R. J. Bergillos, M. Ortega-Sánchez, M. A. Losada, Foreshore evolution of a mixed sand and gravel beach: The case of Playa Granada (Southern Spain), in: Proceedings of the 8th Coastal Sediments, World Scientific, 2015.

[88] R. J. Bergillos, A. López-Ruiz, M. Ortega-Sánchez, G. Masselink, M. A. Losada, Implications of delta retreat on wave propagation and longshore sediment transport-Guadalfeo case study (southern Spain), Marine Geology 382 (2016) 1–16.

[89] R. J. Bergillos, A. López-Ruiz, D. Principal-Gómez, M. Ortega-Sánchez, An integrated methodology to forecast the efficiency of nourishment strategies in eroding deltas, Science of the Total Environment 613 (2018) 1175–1184.

[90] R. J. Bergillos, C. Rodríguez-Delgado, A. López-Ruiz, A. Millares, M. Ortega-Sánchez, M. A. Losada, Recent human-induced coastal changes in the Guadalfeo river deltaic system (southern Spain), in: Proceedings

of the 36th IAHR-International Association for Hydro-Environment Engineering and Research World Congress, 2015.

[91] R. J. Bergillos, C. Rodríguez-Delgado, A. Millares, M. Ortega-Sánchez, M. A. Losada, Impact of river regulation on a Mediterranean delta: Assessment of managed versus unmanaged scenarios, Water Resources Research 52 (2016) 5132–5148.

[92] R. J. Bergillos, M. Ortega-Sánchez, Assessing and mitigating the landscape effects of river damming on the Guadalfeo River delta, southern Spain, Landscape and Urban Planning 165 (2017) 117–129.

[93] R. J. Bergillos, G. Masselink, R. T. McCall, M. Ortega-Sánchez, Modelling overwash vulnerability along mixed sand-gravel coasts with XBeach-G: Case study of Playa Granada, southern Spain, in: Coastal Engineering Proceedings, volume 1, 2016, p. 13.

[94] M. Ortega-Sánchez, R. J. Bergillos, A. López-Ruiz, M. A. Losada, Morphodynamics of Mediterranean Mixed Sand and Gravel Coasts, Springer, 2017.

[95] R. J. Bergillos, M. Ortega-Sánchez, G. Masselink, M. A. Losada, Morpho-sedimentary dynamics of a micro-tidal mixed sand and gravel beach, Playa Granada, southern Spain, Marine Geology 379 (2016) 28–38.

[96] J. Allen, K. Sampanis, J. Wan, D. Greaves, J. Miles, G. Iglesias, Laboratory tests in the development of WaveCat, Sustainability 8 (2016) 1339.

[97] J. Allen, K. Sampanis, J. Wan, J. Miles, D. Greaves, G. Iglesias, Laboratory tests and numerical modelling in the development of WaveCat (2018).

[98] R. J. Bergillos, C. Rodríguez-Delgado, M. Ortega-Sánchez, Advances in management tools for modeling artificial nourishments in mixed beaches, Journal of Marine Systems 172 (2017) 1–13.

[99] L. C. van Rijn, A simple general expression for longshore transport of sand, gravel and shingle, Coastal Engineering 90 (2014) 23 – 39.

[100] R. Pelnard-Considère, Essai de theorie de l'evolution des formes de rivage en plages de sable et de galets, Les Energies de la Mer: Compte Rendu Des Quatriemes Journees de L'hydraulique, Paris 13, 14 and 15 Juin 1956; Question III, rapport 1, 74-1-10 (1956).

[101] R. J. Bergillos, G. Masselink, M. Ortega-Sánchez, Coupling cross-shore and longshore sediment transport to model storm response along a mixed sand-gravel coast under varying wave directions, Coastal Engineering 129 (2017) 93–104.